JACS
JOURNAL OF THE AMERICAN CHEMICAL SOCIETY
pubs.acs.org/JACS
Article

Linking Interfacial Structure and Electrochemical Behaviors of Batteries by High-Resolution Electrocapillarity

Jianwei Lai, Hanrui Zhang, Kang Xu, and Feifei Shi*

Cite This: J. Am. Chem. Soc. 2024, 146, 22257−22265
Read Online
ACCESS | Metrics & More | Article Recommendations | Supporting Information

ABSTRACT: The electrode−electrolyte interface governs the kinetics and reversibility of all electrochemical processes. While theoretical models can calculate and simulate the structure and associated properties of this intriguing component, their validation by direct experimental measurement has been a long-standing challenge. Electrocapillarity is a classical technique that derives the interfacial structure through potential-dependent surface tensions, but its limited resolution has confined its application to ideal systems such as extremely diluted aqueous electrolytes. In this work, we revive this technique with unprecedented time resolution, which allows fast and precise extraction of intrinsic interfacial structure and properties for a wide spectrum of electrolytes, be it ideal or nonideal, aqueous or nonaqueous, dilute or superconcentrated. For the very first time, this new electrocapillarity enables the measurements of a set of interfacial quantities, such as ion concentration distribution and potential drop across Helmholtz planes. Applying it on Zn-battery electrolytes, we discovered that Cl^- specific adsorption at the inner-Helmholtz plane results in unexpected Zn^{2+} aggregation at the outer-Helmholtz plane, and identified such a unique interfacial structure as the fundamental driving force for fast Zn deposition/stripping kinetics and crystallographic texturing. The renaissance of electrocapillarity brings a new tool to the understanding and design of new electrolytes for future battery systems.

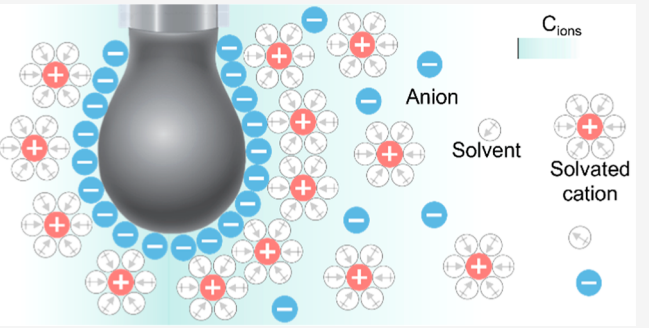

INTRODUCTION

The electrode−electrolyte interface is the core component that distinguishes electrochemistry from conventional chemistry.[1] It governs how ions and solvent molecules accumulate or deplete, as well as how charges are transferred to enable reactions.[2−5] Since both electrode and electrolyte experience a sudden phase discontinuity at the interface, the charge distribution thereat often departs their respective bulk homogeneity, leading to an electrified boundary named the "electric double layer (EDL)".[6] The kinetics and reversibility of most electrochemical processes, e.g., electrostatic adsorption, specific adsorption, metal plating/stripping, intercalation, electrocatalysis, and the formation of permanent interphases, are therefore dictated by the properties and structure of such EDL, which not only constitute the central concept of classical electrochemistry but also carries high significance for advanced battery systems of practical interest.[7−12] The initial electrified interface concept was proposed by Helmholtz in 1853,[13] which was sequentially modified into the well-known EDL models by Gouy,[14] Chapman,[15] Stern[16] (GCS models). Early electrochemical studies in ideal electrolyte systems by Grahame,[17] Bockris,[18] and Conway[19] revealed deviations from these theoretical models and various modifications were made. Thus, far, the majority of our knowledge about the EDL in nonideal electrolytes (e.g., practical battery electrolytes with salt concentrations around 1 molar) has been predominantly reliant on density functional theory calculations and molecular dynamics simulations.[20−22] Experimental verifications of these simulations, however, are pronouncedly absent and are urgently required for modern battery electrolytes.

Various electrochemical techniques have been applied to experimentally characterize EDL properties, such as voltammetry, amperometry, potentiometry,[9] as well as electrochemical impedance spectroscopy (EIS).[23] Traditionally, researchers used to extract differential capacitance via cyclic voltammetry (CV) and EIS, approximating the EDL model as an ideal capacitor or constant phase element.[9] Such assumptions made to accommodate the results from these phenomenological tools work well for ideal electrolyte systems, exemplified by the extremely diluted (<0.001 molar) aqueous solutions of potassium bromide (KBr). However, in most practical battery electrolytes, whose salt concentration resides in the neighborhood of 1.0 molar, ion−ion and ion−solvent interactions far outweigh the ion−electrode interactions, hence

Received: March 17, 2024
Revised: July 9, 2024
Accepted: July 10, 2024
Published: July 16, 2024

https://doi.org/10.1021/jacs.4c03791
J. Am. Chem. Soc. 2024, 146, 22257−22265

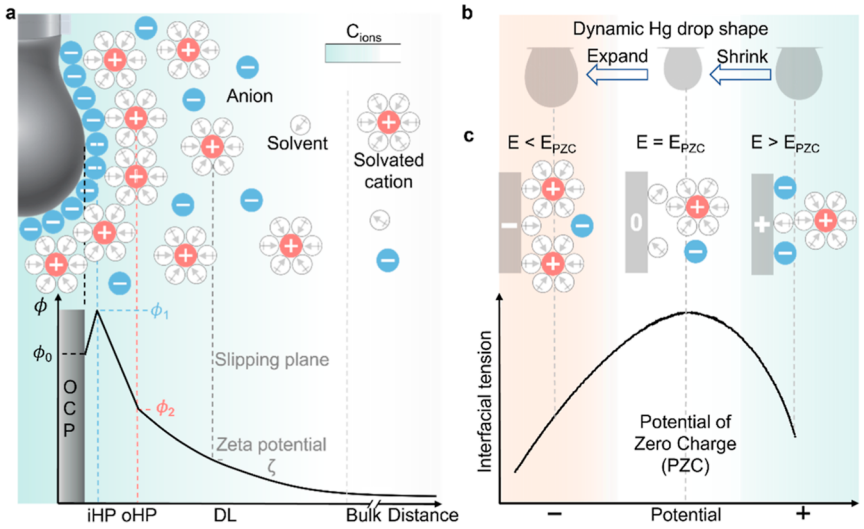

Figure 1. Schematic of high-resolution electrocapillarity. (a) Interfacial structure and associated potential profile at an electrode surface consisting of specifically adsorbed anions in the inner-Helmholtz plane (iHP) and solvated cation in the diffuse layer, under open circuit potential (OCP). iHP refers to the closest approach position of specifically absorbed ions, while outer-Helmholtz plane (oHP) refers to that of nonspecifically adsorbed ions. oHP is the boundary at which the diffuse layer (DL) commences. The EDL hence consists of three substructural regions: an iHP, an oHP, and an adjacent diffuse layer. ϕ_0, ϕ_1, ϕ_2, and ζ represent the potentials at the electrode surface, iHP, oHP, and the slipping plane within the diffuse layer (referenced to the potential in the bulk electrolyte), respectively. (b) Dynamic drop shape of a static mercury electrode (SME) under applied potential. (c) Schematic depiction of interfacial assemblies on the electrode under typical polarization scenarios, and the characteristic potential-tension relation on SME.

complicating the simple picture of pure ion assembly on the interface as expected from ideal electrostatic distributions.[1] This has been reflected by the fact that EDL capacitances extracted from CV or EIS are spread from 10° to 10^2 μF cm^{-2}, dependent on scan rates or frequencies employed[24] (Supporting Discussion 1). To overcome the model assumptions and the indirect phenomenological tools, direct measurement of interfacial parameters becomes crucial. Besides electrochemical techniques, other complementary methods have recently been explored to study the interfacial structure, including sum frequency generation spectroscopy,[25] atomic force microscopy,[26] X-ray reflectivity,[27] and X-ray photoelectron spectroscopy.[28] Electrocapillarity is one such rare technique of direct measurement that is rooted on the Gibbs adsorption isotherm of the interface.[17] It quantifies the interfacial tension of a liquid metal electrode in an electrolyte in response to applied potential, hence revealing a series of key EDL properties.[17,29]

Dropping mercury electrode (DME) was often used in traditional electrocapillarity since the 1920s and is being taught today in electrochemistry textbooks[1,9] (Supporting Discussion 2). However, its governing Tate equation came with two main drawbacks: (1) low accuracy, originated from the oversimplification that the electrolyte densities are negligible compared to that of mercury ($\rho_{electrolyte} \ll \rho_{Hg}$);[30] (2) uncontrollable dropping time (0.5−10 s), which was determined by many fortuitous factors, making it not suitable for practical electrolytes of high viscosity and slow ionic relaxation.[17] The above limitations and the complexity of operation render DME-electrocapillarity nearly forgotten as a research tool since the 1970s.[31] Recently, static mercury electrode (SME) was adopted in ionic liquid systems,[32,33] which extracts interfacial tension from pendant drop shape based on the Young−Laplace fitting[34] (Supporting Discussion 2). Due to the ultraslow relaxation of ionic liquids over hundreds of seconds,[35] less attention has been paid to the time resolution in previous electrocapillarities, thereby impeding the precise curve fitting and more in-depth analysis of intrinsic EDL properties.

In this work, we modernized the electrocapillarity by customizing it with tunable time resolution and verified the new feature in both ideal (0.01−1 M aqueous KBr) and nonideal electrolyte systems [aqueous solutions of 1 and 20 m lithium bis(trifluoromethane sulfonyl)imide, LiTFSI] for benchmarking and comparison. The modernized electrocapillarity demonstrated high data density and accuracy in all of these electrolyte systems. This high-resolution electrocapillarity can achieve 1000 data points V^{-1}, more than 50 times higher than traditional electrocapillarity with 20 points V^{-1}. We further applied this technique to a practical electrolyte with bivalent working ion Zn^{2+} (aqueous solutions of $ZnSO_4$ and $ZnCl_2$) designed for Zn battery chemistries. Due to Cl^- specific adsorption in the inner-Helmholtz plane (iHP), we discovered unexpected enrichment of Zn^{2+} in the EDL region and extracted potential distribution induced by these ions across the Helmholtz planes. Such a special interfacial structure is closely connected to the fast electron transfer kinetics of Zn deposition chemistry and strong texturing along the (101) Zn^0 plane. The significance of this discovery certainly goes beyond Zn chemistry and should be universally applicable in other nonideal battery electrolytes, including nonaqueous systems. In the classical era, only "ideal" electrolytes were studied due to the restrictions of traditional electrocapillarity. This is the very first time that we are using battery electrolyte conditions for electrocapillary tests, thanks to the modernization achieved in this work, which fills a five-decade-old gap. Unrestricted by data density and relaxation time constant, this new high-data-resolution electrocapillarity holds great potential to serve as a universal platform for understanding the complex interfacial structure of diverse electrolyte systems that are critical to future battery chemistries or other electrochemical applications.

https://doi.org/10.1021/jacs.4c03791
J. Am. Chem. Soc. 2024, 146, 22257−22265

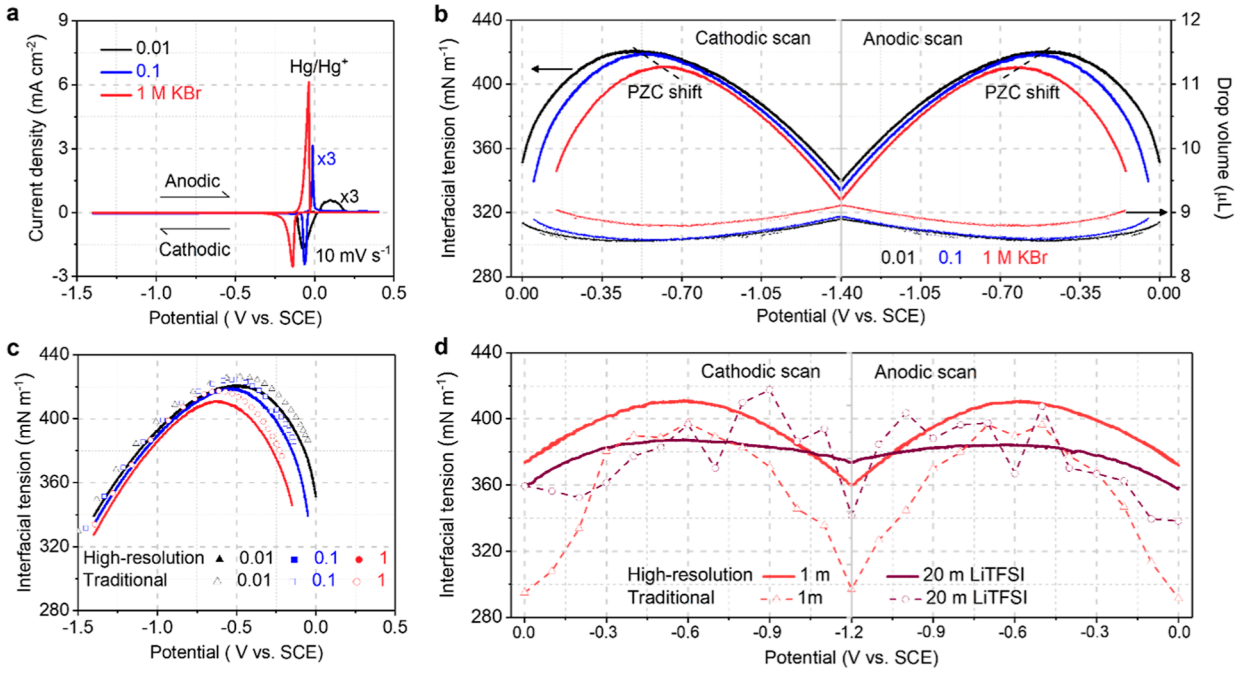

Figure 2. Comparison of high-resolution and traditional electrocapillarity in ideal (0.01−1 M KBr) and nonideal (1 and 20 m LiTFSI) aqueous electrolytes. (a) Synchronous cyclic voltammetry (CV) curves of static mercury electrode (SME) at 10 mV s^{-1} in 0.01, 0.1, and 1 M KBr aqueous electrolytes, which delineates the non-Faradaic region for electrocapillary studies. (b) Perfect symmetry of electrocapillarity in either cathodic or anodic scan and the associated SME volume change. (c) Comparison of electrocapillary data collected by high-resolution (solid symbols) and traditional[40] (hollow symbols) setup in ideal aqueous KBr electrolytes. Reproduced with permission from ref 40. Copyright (1968) Elsevier. (d) Comparison of electrocapillary data in nonideal 1 and 20 m aqueous LiTFSI electrolytes.

RESULTS AND DISCUSSION

Intrinsic Properties of EDL. Most electrocapillary measurements use mercury as the working electrode, due to its liquid state that allows shape change induced by surface tension, wide electrochemical window due to effective suppression of hydrogen evolution, and highly reproducible nature.[9] Here, we customized a pendant mercury setup to study the potential-dependent interfacial free energy. Figure 1a shows the schematic of an interfacial structure with anion specific adsorption and the consequent potential distribution under the open circuit condition. Typically, ions with specific adsorption capability bind tightly with the electrode surface and enrich in the closest vicinity at iHP, while the outer-Helmholtz plane (oHP) is the closest locus of nonspecifically adsorbed counterions with solvation shell (e.g., solvated cations),[17] which sets the boundary for the diffuse layer (DL). The potential at oHP is denoted as ϕ_2, which is a quantity of utmost importance for the interfacial electron transfer kinetics because it determines both the ion concentration in interfacial region and effective electrode potential that the electrolyte is exposed to based on the Frumkin effect.[36] Electrocapillarity is sensitive to the potential at oHP due to the ionic screening effect and abrupt voltage drop of ϕ_2 across EDL. During polarization, the mercury drop first shrinks and then expands when potential is changed from positive to negative ranges, due to the reversible adsorption and desorption at the EDL (Figure 1b). In an ideal electrolyte, a characteristic parabolic-shaped relation emerges between surface tension and applied potential as the signature electrocapillarity curve (Figure 1c), which is often unsymmetric due to the difference in the adsorption behaviors between cation and anion.[1] The potential at the maximum interfacial tension of this curve is called the potential of zero charge (PZC), where the interfacial region houses zero net charges. Either above or below PZC, electrostatic aggregation of ions occurs, thereby weakening the interfacial tension. Further in-depth analysis of electrocapillary curves can deliver more intrinsic EDL properties beyond the PZC and enable us to reconstruct the EDL structure based on the potential profile and interfacial ion distribution.

High-Resolution Electrocapillarity in Ideal and Nonideal Electrolytes. Diluted aqueous solutions of KBr are the most intensively studied ideal electrolytes in classical electrocapillary tests[37] because complete dissociation of ions is expected from such electrolytes with minimum ion pairing.[38] The traditional electrocapillarity is limited by the uncontrollable mercury dropping time, which depends on several factors like mercury flow rate, electrolyte composition, and the associated viscosity and density, and capillary diameter. Therein, each interfacial tension measurement is obtained by averaging at least 10 consecutive drops.[39] Here, we employ aqueous KBr as an established reference to evaluate the new setup. Thanks to the high-resolution capability, we can synchronize both time and voltage resolution during interfacial tension readings, the more experimental details of which are provided in Supporting Discussion 3. To establish the electrochemical stability window within which the electrocapillarity operates, CV is applied to SME in aqueous KBr solutions at salt concentrations across 2 orders of magnitude (0.01−1 M). As the KBr concentration increases, the redox couple current increases, and the potential of Hg/Hg$^+$ negatively shifts accordingly (Figure 2a). We hence selected the non-Faradaic regions that were identified to study the ion accumulation behaviors free from the interference of Faradaic reactions.

https://doi.org/10.1021/jacs.4c03791
J. Am. Chem. Soc. 2024, 146, 22257−22265

Electrocapillary curves in 0.01−1 M KBr aqueous electrolytes and the corresponding volume change of SME are plotted in both cathodic and anodic scans (Figure 2b). Highly symmetric curves obtained in anodic and cathodic scans reveal the ideal reversibility of ion adsorption/desorption in the absence of Faradaic reactions. We further explored the scan-rate effect (10, 50, 100, and 150 mV s^{-1}) on these curves and determined 10 mV s^{-1} as the optimized condition (Supporting Discussion 4). As salt concentration increases from 0.01 to 1 M, PZC negatively shifts from −0.501 to −0.620 V (vs saturated calomel electrode, SCE). Based on the Esin−Markov effect,[41] negatively shifted PZC manifests the specific adsorption of Br^-,[24,42] which binds to mercury surface via a special chemical affinity that is common for most halide ions. To compare the data quality, the cathodic scan of high-resolution results is overlaid with the data obtained via traditional electrocapillarity[37,40] (Figure 2c and Supporting Discussion 5). The latter experiences persistent overestimation in interfacial tension from the Tate equation.[9,30] While both results show a typical asymmetric parabolic shape, high-resolution electrocapillarity exhibits much higher data density (e.g., 1000 points V^{-1}), compared to the traditional one (~20 points V^{-1}).

Higher data density makes in-depth analysis of electrocapillary curves possible, which can provide more intrinsic EDL properties such as interfacial excess charge σ, differential capacitance C_d, and relative surface excess of ions $\Gamma_{\pm(\text{solvent})}$ (Supporting Discussion 6), the quantities that used to be extremely difficult to derive. An optimized eighth-order polynomial regression is employed to fit the raw electrocapillary curves so that these EDL properties can be derived with high accuracy (Supporting Discussion 7). σ, the first derivative of electrocapillary curves, quantifies the net charge of the cation and anion accumulated in the interfacial regions. For example, we obtained the precise relation between σ (i.e., $F\Gamma_{K^+} - F\Gamma_{Br^-}$, F is the Faraday constant) and potential. As concentration increases, total charge increases (Figure S12a). Differential capacitance (C_d), the second derivative of electrocapillary curves, represents the potential-dependent EDL capacitance (Supporting Discussion 8), which increases with electrolyte concentration driven by a greater interfacial ionic population but experiences a hump at ~50 mV positive to E_{PZC} a feature that arises from the interfacial water dipole reorientation under electrostatic polarization.[24,43] To demonstrate the necessity of high-resolution electrocapillarity, the same electrocapillary curve under high (1000 tension V^{-1}) and low (typically 20 tensions V^{-1}) resolution is compared, using 0.01 M KBr as an example. As shown in Figure S13, both interfacial excess charge and capacitance derived from low-resolution electrocapillarity noticeably deviate from the high-resolution curves. Only by exploiting the high-resolution electrocapillarity, we can further extract a series of intrinsic interfacial properties.

Relative surface excess $\Gamma_{\pm(\text{solvent})}$ is defined as the excess concentration of each ion in the interfacial region when compared with their bulk concentration by choosing the solvent (e.g., water) as the reference component, which as a key interfacial property quantifies the ionic distribution as well as the potential drop across the interface. Associated relative surface excess charge [$Z_\pm F\Gamma_{\pm(H_2O)}$, where $Z_\pm$ is the ionic valence with a sign] isolates cation and anion charge contributions from interfacial excess charge σ. To understand the picture of EDL structure, we differentiate the relative surface excess charge of K^+ [$F\Gamma_{K^+(H_2O)}$] and Br^- [$-F\Gamma_{Br^-(H_2O)}$] in 0.1 M KBr (Figure S12c), whose calculation details are provided in Supporting Discussion 6. At PZC, K^+ is in positive excess while Br^- is in negative excess, indicating higher interfacial concentrations for both ions than in the bulk. This phenomenon stems from Br^- specific adsorption at the iHP, which consequently attracts an equal amount of K^+ in the adjacent diffuse layer next to the iHP. By comparing high-resolution and traditional electrocapillarity, we successfully reproduced the intrinsic interfacial properties of ideal KBr electrolytes with high data quality and resolution. As we will show later on, such interfacial structure governed by specific adsorption of one ion in iHP and enrichment of another ion in oHP could carry meaningful significance to charge transfer for cell reactions.

Besides the data resolution, high-resolution electrocapillarity also has the advantage of being able to measure nonideal battery electrolyte systems of higher viscosity and longer ionic relaxation time, such as the extreme case of superconcentrated aqueous electrolyte, the water-in-salt electrolytes (WiSE) consisting of 20 molal LiTFSI in water.[44] In Figure 2d and Supporting Discussion 9, we compare our high-resolution and traditional DME setup in such nonideal Li^+ battery electrolytes (i.e., 1 and 20 m aqueous LiTFSI). The error bar of traditional electrocapillarity repeated 10 times per data point is ~94 mN m^{-1}, taking 1 m aqueous LiTFSI as an example (Figure S16). However, the error bar of high-resolution electrocapillarity repeated 3 times per point is ~9 mN m^{-1}, which is reduced by 10 times compared to the traditional one. Concentrated aqueous electrolytes based on LiTFSI with a large anion size, high viscosity, and strong ion pairing make it deviate far from ideality. Traditional electrocapillarity is severely plagued by the large fluctuation in interfacial tensions, due to the uncontrollable lifetime of DME (Figure 2d). Typical DME lifetime is only ~3 s even for 20 m aqueous LiTFSI, which is lower than its relaxation time over 4 s (Supporting Discussion 9). The sluggish ionic relaxation, together with a high electrolyte density of 1.702 g cm^{-3}, renders the traditional method with high inaccuracies. On the other hand, the high-resolution method can provide reliable potential-interfacial tension relation. The higher interfacial tension at ~ −1.2 V in 20 m compared to 1 m LiTFSI electrolyte may result from a looser electrical double layer (EDL) with lower charge density.[45] The thicker EDL in 20 m LiTFSI indicates that interfacial ions are more loosely packed near the interface, leading to an increase in the interfacial tension. Unrestricted by data density and relaxation time constant, this approach demonstrates the universality for almost any nonideal electrolytes that is of interest to practical electrochemical devices including advanced batteries.

EDL Behaviors of Practical Zn Electrolytes. We applied this high-resolution electrocapillarity on nonideal electrolytes in an attempt to decipher the relation between the interfacial behaviors and electrochemical performances in actual batteries. Aqueous solutions of $ZnSO_4$ and $ZnCl_2$ are chosen here not only because Zn battery research has been active in the past decade as a viable alternative to lithium-ion batteries in energy storage market for its low cost and earth-abundant nature,[46,47] but more importantly because electrolytes containing bivalent working ions such as Zn^{2+} often reside far away from ideality due to the extremely strong Coulombic field they carry, hence

https://doi.org/10.1021/jacs.4c03791
J. Am. Chem. Soc. 2024, 146, 22257−22265

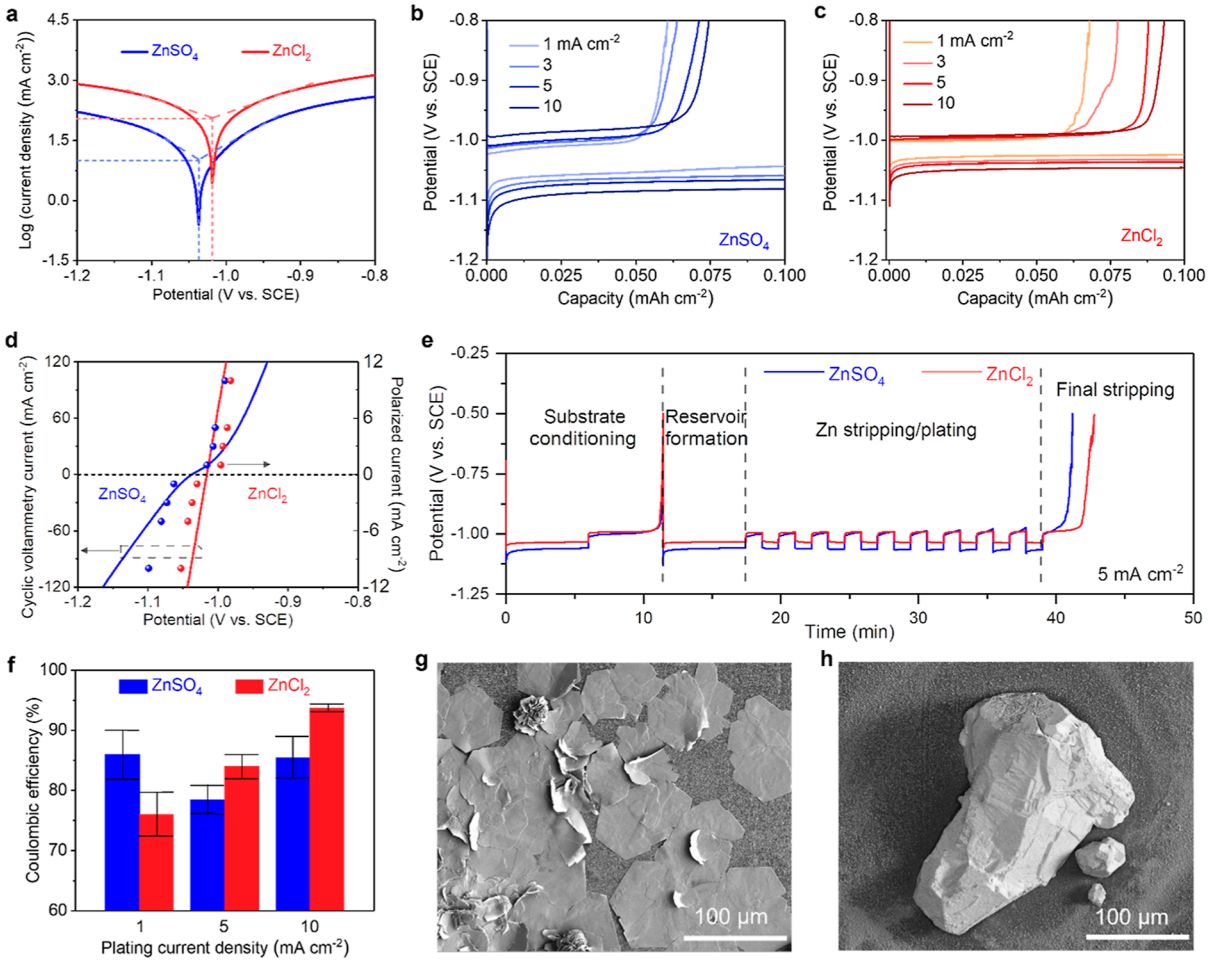

Figure 3. Anion effect on the electrochemical behaviors of practical Zn battery electrolytes (1 M aqueous $ZnSO_4$ and $ZnCl_2$) using a model glassy carbon electrode. (a) Tafel plots of Zn deposition/stripping at the optimized scan rate of 10 V s^{-1} after *iR* compensation. (b,c) Polarization behaviors in $ZnSO_4$ and $ZnCl_2$ under various current densities of 1, 3, 5, and 10 mA cm^{-2} for 0.1 mA h cm^{-2}. (d) Comparison of current−potential plots from CV and polarization curves. The overpotentials from polarization tests are obtained at a capacity of 0.04 mA h cm^{-2}. (e) Average Coulombic efficiency (CE) of Zn plating/stripping at 5 mA cm^{-2} using the "reservoir half-cell" galvanostatic protocol. (f) Effect of harsh current density conditions (1, 5, and 10 mA cm^{-2}) on the average CE. (g,h) SEM images of electrodeposited Zn at 0.1 mA cm^{-2} for 1 mA h cm^{-2} in (g) $ZnSO_4$ and (h) $ZnCl_2$.

they represent the most challenging scenario to traditional electrocapillarity.[48] A glassy carbon electrode (GC) is used as model solid electrode due to its reproducibility, chemical inertness, and absence of orientation effect. The exchange current densities in 1 M $ZnSO_4$ and $ZnCl_2$ were measured by CV tests, and 10 V s^{-1} was determined to be the optimum scan rate to extract exchange current (Supporting Discussion 10). Tafel plots of 1 M $ZnSO_4$ and $ZnCl_2$ report the exchange current as 109.6 mA cm^{-2} in 1 M $ZnCl_2$ and 9.8 mA cm^{-2} in 1 M $ZnSO_4$ (Figure 3a). The substantially higher exchange current, by an order of magnitude, in $ZnCl_2$ reflects much faster electron transfer kinetics at the interface and strongly implies a different mechanism governed by the unique interfacial structure. Polarization behaviors of Zn electrolytes were further evaluated by galvanostatic tests (Figure 3b,c), where both deposition and stripping overpotentials in 1 M $ZnCl_2$ are correspondingly lower than those in $ZnSO_4$ at current densities from 1 to 10 mA cm^{-2}. Faster electron transfer kinetics in the $ZnCl_2$ electrolyte is thus firmly established by both the CV and galvanostatic experiment when these data are plotted in a Butler−Volmer manner (Figure 3d). Similar accelerated electrode kinetics had been reported for other redox reactions like Bi/Bi^{3+} with Cl^-, but to our best knowledge, no efforts have been made to shed lights on the fundamental mechanism underneath.[49]

To connect the electron transfer kinetics to the reversibility of the Zn anode, we examined the average Coulombic efficiency (CE) and the Zn^0 deposition morphology. The "reservoir half-cell" galvanostatic protocol[50] is employed (Figure 3e and Supporting Discussion 11). Each plating current condition is repeated three times. In the $ZnSO_4$ electrolyte, CE becomes lower at higher plating current, reflecting that charge transfer across interface fails to supply sufficient Zn^{2+} for the Zn^0 deposition. The higher Coulombic efficiency in $ZnSO_4$ at 10 mA cm^{-2} compared to 5 mA cm^{-2} is attributed to the reduced time for the parasitic reactions, consistent with the literature.[51] However, in $ZnCl_2$ electrolyte, a higher current always results in higher CE, which is counterintuitive from an interfacial kinetics perspective because there are essentially no parasitic reactions in the selected non-Faradaic potential range (Figure 3f). To understand this unusual behavior of the CE-rate relation, we further checked the Zn^0 deposit morphology (Figure 3g−h and Supporting Discussion 12). The electrodeposits from 1 M

https://doi.org/10.1021/jacs.4c03791
J. Am. Chem. Soc. 2024, 146, 22257−22265

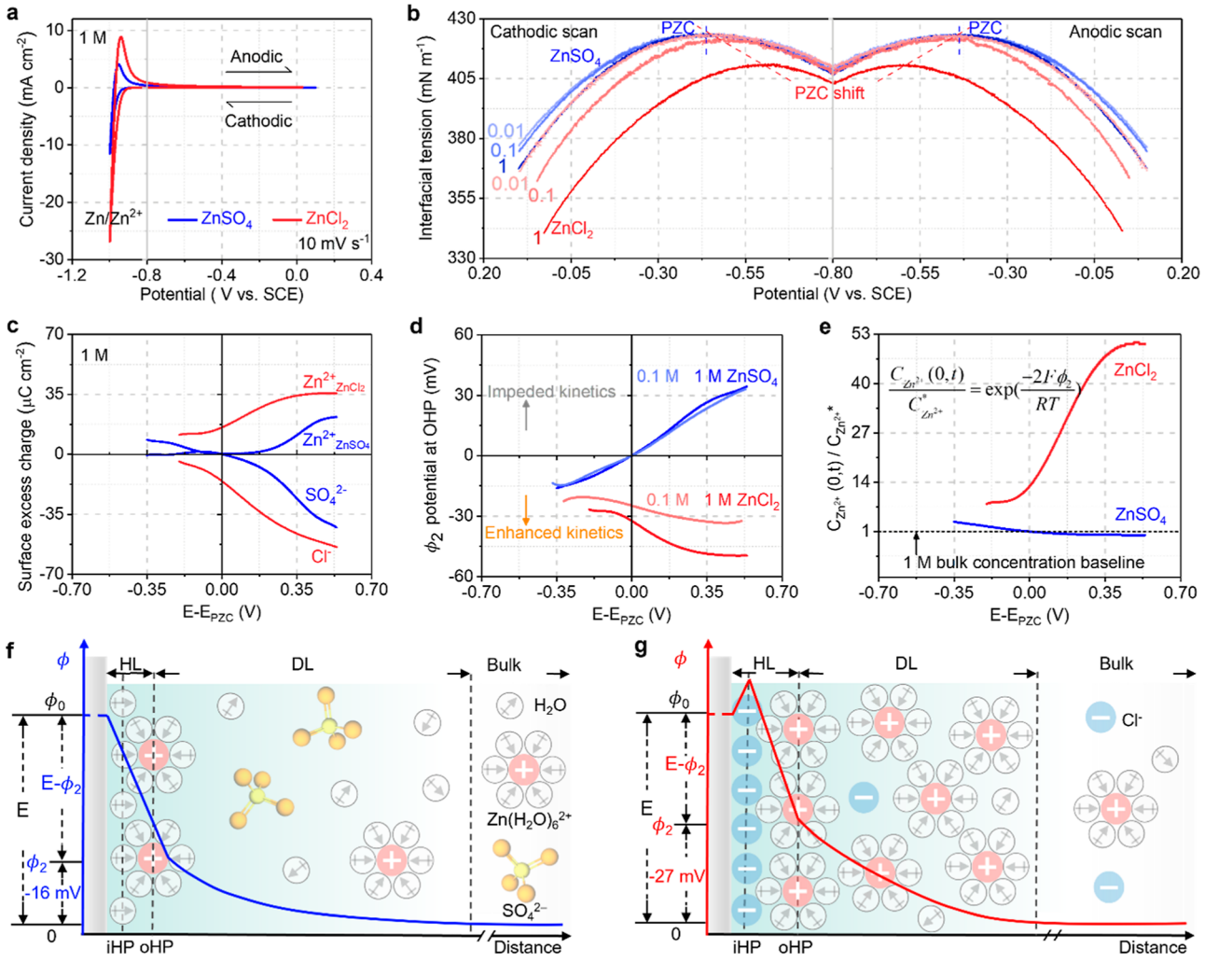

Figure 4. Correlating interfacial structure and electron transfer kinetics in aqueous $ZnSO_4$and $ZnCl_2$electrolytes. (a) Synchronous cyclic voltammetry (CV) curves of SME at 10 mV s^{-1} in 1 M $ZnSO_4$ and $ZnCl_2$. (b) Corresponding cathodic and anodic scan of high-resolution electrocapillary curves. (c) Relative surface excess charge of Zn^{2+}, SO_4^{2-}, and Cl^- in 1 M $ZnSO_4$ and $ZnCl_2$. (d) Quantification of ϕ_2 the potential at the outer Helmholtz plane in 0.1 and 1 M $ZnSO_4$ and $ZnCl_2$. (e) Ratio of interfacial Zn^{2+} concentration $[C_{zn}^{2+}(0, t)]$ to its bulk (C_{zn}^{2+*}) in 1 M $ZnSO_4$ and $ZnCl_2$, derived from the Boltzmann distribution with ϕ_2. (f–g) Schematic of the interfacial structure for (f) $ZnSO_4$ and (g) $ZnCl_2$ at −0.8 V (vs SCE), based on their interfacial properties. −0.8 V is chosen as a representative negative potential before the Zn^{2+} reduction reaction happens. Potential ϕ is referenced to the potential in the bulk electrolyte.

$ZnSO_4$ electrolytes experience a transition from flake to mossy structure as the plating current increases. In 1 M $ZnCl_2$, however, faceted ball-shaped deposits are observed in a wide range of current densities. Under X-ray powder diffraction (XRD), the crystallographic orientation of Zn^0 deposits from $ZnSO_4$ are found to expose (002) basal plane, while (101) crystalline plane is dominant on the Zn^0 deposits from $ZnCl_2$ electrolyte (Figure S21). Such preference of (101) crystalline plane texturing deviates from the thermodynamically favored (002) Wulff structure[52] (Supporting Discussion 13). Such different electrochemical behaviors in $ZnSO_4$ and $ZnCl_2$ electrolytes, governed by the interfacial structures in these two electrolytes, apparently have significant consequences on the battery performance.

Deciphering EDL Structure of Zn Electrolytes. CV curves of SME in 0.01−1 M aqueous $ZnSO_4$ and $ZnCl_2$ are plotted in Figure 4a and Supporting Discussion 14, in which the redox reaction of Zn−Hg alloying/dealloying initiates below −0.8 V (vs SCE) for both electrolytes, with $ZnCl_2$ exhibiting a higher redox current. Supporting Discussion 15 shows the associated Tafel plot, where $ZnCl_2$ exhibits a higher equilibrium potential (−0.966 V) and exchange current (4.6 mA cm^{-2}) compared to that of $ZnSO_4$ (−0.976 V and 1.9 mA cm^{-2}). Regardless of electrode materials and testing methods, all evidence points toward an accelerated charge transfer kinetics in $ZnCl_2$ during Zn deposition/stripping or alloying/dealloying. Figure 4b shows the synchronized electrocapillary curves with CV in 1 M $ZnSO_4$ and $ZnCl_2$. What reveals more detailed information is the PZC location on electrocapillary curves, which in 0.01−1 M $ZnSO_4$ remains almost constant ~ −0.438 V (vs SCE), while in $ZnCl_2$ it negatively shifts from −0.449 to −0.601 V (PZC are summarized in Table S3). As in the case with aqueous KBr (Figure 2b), the negatively shifted PZC represents the specific adsorption of Cl^-.[17,53] Due to this specific adsorption, the interfacial tension in 1 M $ZnCl_2$ is ~15 mN m^{-1} lower than that in 1 M $ZnSO_4$ at their respective PZC.

From the electrocapillarity of high precision, we first extracted the interfacial excess charge σ, which is higher in 1 M $ZnCl_2$ over $ZnSO_4$ at $E < E_{PZC}$ (Supporting Discussion 16).

https://doi.org/10.1021/jacs.4c03791
J. Am. Chem. Soc. 2024, 146, 22257−22265

Based on the electrocapillary governing equation (Supporting Discussion 6), we quantified their relative surface excess charge $[2F\Gamma_{Zn^{2+}(H_2O)}, -2F\Gamma^{2-}_{SO_4(H_2O)}, -F\Gamma_{Cl^-(H_2O)}]$ in Figure 4c. After referencing PZC conditions, relative surface excesses of both cation and anion are higher in 1 M $ZnCl_2$, suggesting an interfacial region significantly enriched with both Zn^{2+} and Cl^- ions in $ZnCl_2$. At PZC, 1 M $ZnSO_4$ possesses zero relative surface excess charge due to nonspecific adsorption, while 1 M $ZnCl_2$ exhibits cation and anion excess under Cl^- specific adsorption. To resolve the fine structure of such interface, we further differentiated the relative surface excess charge of Cl^- in the iHP and the diffuse layer, by coupling our experimental data and the GCS theory.[17,54] The calculation details are provided in Supporting Discussion 17. Excess Cl^- is found in iHP, whereas a deficiency in Cl^- concentration follows in the adjacent diffuse layer, resulting in a local enrichment of Zn^{2+} (Supporting Discussion 18). It should be mentioned that such a breach of electroneutrality between cation and anion species is allowed in the interfacial regions due to the nature of the EDL[1]. The aforementioned interfacial properties, including the unusual kinetics of Zn^{2+} deposition chemistry, must be direct consequences of this fine structure.

Based on the in-depth analysis of high-resolution electrocapillary data that were never available before, we can now reconstruct the EDL structure along with key properties, including the potential profile and ion distribution across the interface as well as the associated thickness dimension. Among these properties, the potential at OHP ϕ_2 is of utmost importance because it directly dictates the charge transfer kinetics across the interface, but its precise measurement has never been made due to the absence of a technique that must be simultaneously precise, high-resolution and yet operando in nature. According to the kinetics theory,[9,36] the charge transfer rate across an interface depends on two factors: (1) the effective concentration of the reactant species (Zn^{2+}) at the interface, and (2) the driving force, which is the potential difference across the interface. Thus, ϕ_2 affects the charge transfer kinetics of Zn deposition reaction in two corresponding aspects[36] (Supporting Discussion 19): first, by the interfacial Zn^{2+} concentration $[C_{ions}(0, t)]$, which significantly differs from its bulk concentration C_r^* depending on the applied potential; second, the effective potential difference driving this reduction, $E-\phi_2$ instead of the potential applied on the cell E. Thus, the driving overpotential is $E - E^{0\prime} - \phi_2$ (where E is the electrode potential and $E^{0\prime}$ the formal potential).[24,53] As early as 1933,[36] Frumkin first recognized such correlation between EDL structure and electrode kinetics, so the combined effect has been known as the "Frumkin effect", but the relation was never quantified for practical electrolyte systems.[24,36]

In Figure 4d, we first derived the potential at the OHP ϕ_2, and found it to be more negative in $ZnCl_2$ than in $ZnSO_4$ due to Cl^- specific adsorption at the IHP. ϕ_2 is very sensitive to the specific adsorption of Cl^-, while in $ZnSO_4$ it is barely affected in the absence of specifical adsorption. Besides the potential profile, we further derived interfacial ion distribution based on the Boltzmann distribution[9] with ϕ_2. Notably, for the high-resolution electrocapillary measurements of 1 M $ZnSO_4$ and $ZnCl_2$ electrolytes, each continuous scan was repeated three times. As shown in Figure S23, the repeated electrocapillary curves exhibit near-perfect overlap, with an error bar of 0.3 mN m^{-1}. Consequently, the error bar for the extracted outer Helmholtz potential is less than 1 mV. Given the negligible magnitude of this error, it is not incorporated into the figure. Figure 4e shows the ratio of interfacial Zn^{2+} concentration $[C_{zn}^{2+}(0, t)]$ to its bulk (C_{zn}^{2+}*), denoted as $C_{zn}^{2+}(0, t)/C_{zn}^{2+}$*, in both 1 M $ZnSO_4$ and $ZnCl_2$. Induced by Cl^- specific adsorption, $C_{zn}^{2+}(0, t)$ is two times higher concentrated in $ZnCl_2$ than $ZnSO_4$ (8 over 3 M) at −0.8 V (vs SCE), which for the first time explains how the relative surface excess charge affects the charge transfer kinetics in a practical electrolyte. The accelerated reaction rate and unique morphology of Zn^0 are the consequences of the combined effects of a more negative ϕ_2 and high interfacial concentration of Zn^{2+} near the Helmholtz planes (Supporting Discussion 20). Moreover, we also found that the EDL thickness in $ZnCl_2$ is smaller than in $ZnSO_4$, due to the higher relative surface excesses and differential capacitance at $E < E_{PZC}$ (Figure 4c and Supporting Discussion 16). The root cause of different interfacial structures is the specific adsorption of Cl^- versus the nonspecific adsorption of SO_4^{2-}, as evidenced from their respective PZC in Figure 4b. Cl^- ions bind tightly with the electrode surface and enrich in the inner Helmholtz plane, while SO_4^{2-}resides beyond the outer Helmholtz plane and locates in the diffuse layer.

Figure 4f–g schematically shows the reconstructed EDL structures in 1 M $ZnSO_4$ and $ZnCl_2$ electrolyte at −0.8 V (vs SCE). For $ZnSO_4$, the potential profile monotonically decreases, resulting in a less negative ϕ_2 of −16 mV, while in the presence of Cl^--specific adsorption of $ZnCl_2$, a negative ϕ_2 of −27 mV accelerates the Zn^{2+}-migration across the interface. Interfacial ion distribution also manifests the unexpected Zn^{2+} aggregation near Helmholtz planes driven by Cl^- specific adsorption. Due to the higher interfacial Zn^{2+} concentration, the EDL becomes more compact. Such in-depth knowledge derived from this new high-resolution electrocapillarity certainly carries its significance far beyond Zn electrolytes or even batteries because it adds a tool that allows us to reconstruct the extremely important but extremely sensitive interfacial structures that essentially govern all electrochemical devices.

CONCLUSIONS

In this work, we modernized electrocapillarity by making it high-resolution and capable of high accuracy. The new electrocapillarity now makes it possible to derive a series of interfacial information that was unavailable previously in classical electrochemistry. Applying this tool to practical Zn battery electrolytes, we systematically reveal how the EDL structure governs electrochemical behaviors, such as exchange current, polarization overpotential, Coulombic efficiency, and morphological orientation of electrodeposited Zn^0. In particular, we quantified how the ϕ_2 of the OHP can serve as a critical descriptor to dictate interfacial electron transfer kinetics and their consequences in Zn^0 deposition morphology. The knowledge obtained highlights the possibility of electrolyte engineering via designed anion specific adsorption. This revived electrocapillarity technique will serve as a universal platform to derive the interfacial structure and even predict electrochemical behaviors for diverse electrolyte systems, such as nonaqueous, solvent-in-salt, and molten salt electrolytes.

https://doi.org/10.1021/jacs.4c03791
J. Am. Chem. Soc. 2024, 146, 22257−22265

■ ASSOCIATED CONTENT

Data Availability Statement

All data is available in the manuscript or the Supporting Information.

Supporting Information

The Supporting Information is available free of charge at https://pubs.acs.org/doi/10.1021/jacs.4c03791.

Method of electrochemical and materials characterizations, electrode calibration for interfacial tension measurement, photographs of experimental setup, derivation of interfacial properties from electrocapillarity, SEM images, XRD patterns, and extraction of outer Helmholtz potential ϕ_2 (PDF)

■ AUTHOR INFORMATION

Corresponding Author

Feifei Shi − *John and Willie Leone Family Department of Energy and Mineral Engineering, Pennsylvania State University, University Park, Pennsylvania 16802, United States;* orcid.org/0000-0002-2598-1867; Email: feifeishi@psu.edu

Authors

Jianwei Lai − *John and Willie Leone Family Department of Energy and Mineral Engineering, Pennsylvania State University, University Park, Pennsylvania 16802, United States;* orcid.org/0000-0001-5841-1134

Hanrui Zhang − *John and Willie Leone Family Department of Energy and Mineral Engineering, Pennsylvania State University, University Park, Pennsylvania 16802, United States;* orcid.org/0000-0001-8576-9705

Kang Xu − *SES AI Corporation, Woburn, Massachusetts 01801, United States*

Complete contact information is available at: https://pubs.acs.org/10.1021/jacs.4c03791

Funding

J.L. and F.S. thank the support from the U.S. Department of Energy under contract DE-NE0009286 and the National Science Foundation under grant no. 2239690. H.Z. and F.S. were partially supported by the Assistant Secretary for Energy Efficiency and Renewable Energy, Office of Vehicle Technologies of the US Department of Energy through the Advanced Battery Materials Research Program.

Notes

The authors declare no competing financial interest.

■ REFERENCES

(1) Xu, K. *Electrolytes, Interfaces and Interphases: Fundamentals and Applications in Batteries*. Royal Society of Chemistry, 2023; pp 131−191.

(2) Xu, J.; Zhang, J.; Pollard, T. P.; Li, Q.; Tan, S.; Hou, S.; Wan, H.; Chen, F.; He, H.; Hu, E.; et al. Electrolyte design for Li-ion batteries under extreme operating conditions. *Nature* **2023**, *614* (7949), 694−700.

(3) Meng, Y. S.; Srinivasan, V.; Xu, K. Designing better electrolytes. *Science* **2022**, *378* (6624), No. eabq3750.

(4) Xu, K. Electrolytes and interphases in Li-ion batteries and beyond. *Chem. Rev.* **2014**, *114* (23), 11503−11618.

(5) Bard, A. J.; Abruna, H. D.; Chidsey, C. E.; Faulkner, L. R.; Feldberg, S. W.; Itaya, K.; Majda, M.; Melroy, O.; Murray, R. W. The electrode/electrolyte interface-a status report. *J. Phys. Chem.* **1993**, *97* (28), 7147−7173.

(6) Devanathan, M.; Tilak, B. The structure of the electrical double layer at the metal-solution interface. *Chem. Rev.* **1965**, *65* (6), 635−684.

(7) Armand, M.; Tarascon, J.-M. Building better batteries. *nature* **2008**, *451* (7179), 652−657.

(8) Stamenkovic, V. R.; Strmcnik, D.; Lopes, P. P.; Markovic, N. M. Energy and fuels from electrochemical interfaces. *Nat. Mater.* **2017**, *16* (1), 57−69.

(9) Bard, A. J.; Faulkner, L. R.; White, H. S. *Electrochemical Methods: Fundamentals and Applications*; John Wiley & Sons, 2022.

(10) Schmickler, W.; Santos, E. *Interfacial Electrochemistry*; Springer Science & Business Media, 2010.

(11) Lück, J.; Latz, A. Modeling of the electrochemical double layer and its impact on intercalation reactions. *Phys. Chem. Chem. Phys.* **2018**, *20* (44), 27804−27821.

(12) Dunn, B.; Kamath, H.; Tarascon, J.-M. Electrical energy storage for the grid: a battery of choices. *Science* **2011**, *334* (6058), 928−935.

(13) Helmholtz, H. v. Ueber einige Gesetze der Vertheilung elektrischer Ströme in körperlichen Leitern, mit Anwendung auf die thierisch-elektrischen Versuche (Schluss.). *Ann. Phys.* **1853**, *165* (7), 353−377.

(14) Gouy, M. Sur la constitution de la charge électrique à la surface d'un électrolyte. *J. Phys. Theor. Appl.* **1910**, *9* (1), 457−468.

(15) Chapman, D. L. LI. A contribution to the theory of electrocapillarity. *London, Edinburgh Dublin Phil. Mag. J. Sci.* **1913**, *25* (148), 475−481.

(16) Stern, O. Zur theorie der elektrolytischen doppelschicht. *Z. Elektrochem. Angew. Phys. Chem.* **1924**, *30* (21−22), 508−516.

(17) Grahame, D. C. The electrical double layer and the theory of electrocapillarity. *Chem. Rev.* **1947**, *41* (3), 441−501.

(18) Bockris, J. M.; Devanathan, M.; Müller, K. On the Structure of Charged interfaces. In *Electrochemistry*; Elsevier, 1965; pp 832−863.

(19) Conway, B. E. Transition from "supercapacitor" to "battery" behavior in electrochemical energy storage. *J. Electrochem. Soc.* **1991**, *138* (6), 1539−1548.

(20) Wu, J. Understanding the electric double-layer structure, capacitance, and charging dynamics. *Chem. Rev.* **2022**, *122* (12), 10821−10859.

(21) Yu, Y.-X.; Wu, J.; Gao, G.-H. Density-functional theory of spherical electric double layers and ζ potentials of colloidal particles in restricted-primitive-model electrolyte solutions. *J. Chem. Phys.* **2004**, *120* (15), 7223−7233.

(22) Burt, R.; Birkett, G.; Zhao, X. A review of molecular modelling of electric double layer capacitors. *Phys. Chem. Chem. Phys.* **2014**, *16* (14), 6519−6538.

(23) Gharbi, O.; Tran, M. T.; Tribollet, B.; Turmine, M.; Vivier, V. Revisiting cyclic voltammetry and electrochemical impedance spectroscopy analysis for capacitance measurements. *Electrochim. Acta* **2020**, *343*, 136109.

(24) Conway, B. E. *Electrochemical Supercapacitors: Scientific Fundamentals and Technological Applications*; Springer Science & Business Media, 2013.

(25) Rehl, B.; Ma, E.; Parshotam, S.; DeWalt-Kerian, E. L.; Liu, T.; Geiger, F. M.; Gibbs, J. M. Water structure in the electrical double layer and the contributions to the total interfacial potential at different surface charge densities. *J. Am. Chem. Soc.* **2022**, *144* (36), 16338−16349.

(26) Legg, B. A.; Baer, M. D.; Chun, J.; Schenter, G. K.; Huang, S.; Zhang, Y.; Min, Y.; Mundy, C. J.; De Yoreo, J. J. Visualization of aluminum ions at the mica water interface links hydrolysis state-to-surface potential and particle adhesion. *J. Am. Chem. Soc.* **2020**, *142* (13), 6093−6102.

(27) Lee, S. S.; Koishi, A.; Bourg, I. C.; Fenter, P. Ion correlations drive charge overscreening and heterogeneous nucleation at solid-aqueous electrolyte interfaces. *Proc. Natl. Acad. Sci. U.S.A.* **2021**, *118* (32), No. e2105154118.

(28) Brown, M. A.; Abbas, Z.; Kleibert, A.; Green, R. G.; Goel, A.; May, S.; Squires, T. M. Determination of surface potential and

electrical double-layer structure at the aqueous electrolyte-nanoparticle interface. *Phys. Rev. X* **2016**, *6* (1), 011007.
(29) Grahame, D. C.; Whitney, R. B. The Thermodynamic Theory Of Electrocapillarity1. *J. Am. Chem. Soc.* **1942**, *64* (7), 1548−1552.
(30) Kadis, R.; Chunovkina, A. Electrocapillary measurements by drop-time technique: Comparison of calibration methods. *Measurement* **2016**, *90*, 110−117.
(31) Payne, R. The electrical double layer: Problems and recent progress. *J. Electroanal. Chem. Interfacial Electrochem.* **1973**, *41* (2), 277−309.
(32) Nishi, N.; Hashimoto, A.; Minami, E.; Sakka, T. Electrocapillarity and zero-frequency differential capacitance at the interface between mercury and ionic liquids measured using the pendant drop method. *Phys. Chem. Chem. Phys.* **2015**, *17* (7), 5219−5226.
(33) Nishi, N.; Yasui, S.; Hashimoto, A.; Sakka, T. Anion dependence of camel-shape capacitance at the interface between mercury and ionic liquids studied using pendant drop method. *J. Electroanal. Chem.* **2017**, *789*, 108−113.
(34) Bashforth, F.; Adams, J. C. *An Attempt to Test the Theories of Capillary Action by Comparing the Theoretical and Measured Forms of Drops of Fluid*; University Press, 1883.
(35) Wang, Y.-L.; Li, B.; Sarman, S.; Mocci, F.; Lu, Z.-Y.; Yuan, J.; Laaksonen, A.; Fayer, M. D. Microstructural and dynamical heterogeneities in ionic liquids. *Chem. Rev.* **2020**, *120* (13), 5798−5877.
(36) Frumkin, A. wasserstoffüberspannung und struktur der doppelschicht. *Z. Phys. Chem.* **1933**, *164A* (1), 121−133.
(37) Devanathan, M.; Peries, P. The adsorption of potassium halides at the mercury/water interface. *Trans. Faraday Soc.* **1954**, *50*, 1236−1243.
(38) Borodin, O.; Self, J.; Persson, K. A.; Wang, C.; Xu, K. Uncharted waters: super-concentrated electrolytes. *Joule* **2020**, *4* (1), 69−100.
(39) Meites, L.; Sturtevant, J. M. Automatic Drop Timer for Use with Dropping Mercury Electrodes. *Anal. Chem.* **1952**, *24* (7), 1183−1184.
(40) Lawrence, J.; Parsons, R.; Payne, R. Adsorption of halides at the mercury-water interface. *J. Electroanal. Chem. Interfacial Electrochem.* **1968**, *16* (2), 193−206.
(41) Esin, O.; Markov, B. *Acta Physicochen*; USSR, 1939; Vol. *10*, p 353.
(42) Schmickler, W.; Guidelli, R. The partial charge transfer. *Electrochim. Acta* **2014**, *127*, 489−505.
(43) Ojha, K.; Doblhoff-Dier, K.; Koper, M. T. Double-layer structure of the Pt (111)-aqueous electrolyte interface. *Proc. Natl. Acad. Sci. U.S.A.* **2022**, *119* (3), No. e2116016119.
(44) Suo, L.; Borodin, O.; Gao, T.; Olguin, M.; Ho, J.; Fan, X.; Luo, C.; Wang, C.; Xu, K. Water-in-salt" electrolyte enables high-voltage aqueous lithium-ion chemistries. *Science* **2015**, *350* (6263), 938−943.
(45) Smith, A. M.; Lee, A. A.; Perkin, S. The electrostatic screening length in concentrated electrolytes increases with concentration. *J. Phys. Chem. Lett.* **2016**, *7* (12), 2157−2163.
(46) Chen, S.; Zhang, M.; Zou, P.; Sun, B.; Tao, S. Historical development and novel concepts on electrolytes for aqueous rechargeable batteries. *Energy Environ. Sci.* **2022**, *15*, 1805−1839.
(47) Zhang, T.; Tang, Y.; Guo, S.; Cao, X.; Pan, A.; Fang, G.; Zhou, J.; Liang, S. Fundamentals and perspectives in developing zinc-ion battery electrolytes: a comprehensive review. *Energy Environ. Sci.* **2020**, *13* (12), 4625−4665.
(48) Wang, F.; Borodin, O.; Gao, T.; Fan, X.; Sun, W.; Han, F.; Faraone, A.; Dura, J. A.; Xu, K.; Wang, C. Highly reversible zinc metal anode for aqueous batteries. *Nat. Mater.* **2018**, *17* (6), 543−549.
(49) Randles, J.; Somerton, K. Kinetics of rapid electrode reactions. Part 4.—Metal ion exchange reaction at amalgam electrodes. *Trans. Faraday Soc.* **1952**, *48*, 951−955.
(50) Ma, L.; Schroeder, M. A.; Borodin, O.; Pollard, T. P.; Ding, M. S.; Wang, C.; Xu, K. Realizing high zinc reversibility in rechargeable batteries. *Nat. Energy* **2020**, *5* (10), 743−749.
(51) Dong, N.; Zhang, F.; Pan, H. Towards the practical application of Zn metal anodes for mild aqueous rechargeable Zn batteries. *Chem. Sci.* **2022**, *13* (28), 8243−8252.
(52) Zheng, J.; Archer, L. A. Controlling electrochemical growth of metallic zinc electrodes: Toward affordable rechargeable energy storage systems. *Sci. Adv.* **2021**, *7* (2), No. eabe0219.
(53) Bard, A. J.; Faulkner, L. R. Fundamentals and applications: electrochemical methods. *Electrochemical Methods*; Wiley, 2001; Vol. *2*, p 482.
(54) Grahame, D. C. Diffuse double layer theory for electrolytes of unsymmetrical valence types. *J. Chem. Phys.* **1953**, *21* (6), 1054−1060.

https://doi.org/10.1021/jacs.4c03791
J. Am. Chem. Soc. 2024, 146, 22257−22265